Generalized parameter-space metrics for continuous gravitational-wave searches

P. B. Covas[1,2,*] and R. Prix[1]

[1]*Max Planck Institute for Gravitational Physics (Albert Einstein Institute) and Leibniz Universität Hannover, D-30167 Hannover, Germany*

[2]*Departament de Física, Universitat de les Illes Balears, IAC3—IEEC, Carretera Valldemossa km 7.5, E-07122 Palma, Spain*

(Received 28 March 2025; accepted 16 July 2025; published 21 August 2025)

Many searches for continuous gravitational waves face significant computational challenges due to the need to explore large parameter spaces characterized by unknown parameters. Parameter-space metrics are used to predict the relative loss of signal power when the searched parameters differ from the true signal parameters. In this paper, we present generalized parameter-space metrics for the $\mathcal{F}$-statistic (a detection statistic used in many searches) that improve upon previous idealized metrics by incorporating realistic effects such as data gaps and varying noise floors. We derive a new marginalized $\mathcal{F}$-statistic metric that is more accurate than the previous averaged $\mathcal{F}$-statistic metric, especially for short coherent segments. We also derive a more accurate semicoherent metric that properly accounts for the signal-power variability over segments. We provide numerical tests illustrating that the new generalized metrics provide more accurate mismatch predictions than previous expressions. More accurate metrics can result in a reduced number of templates needed for a given search, a feature that could improve the sensitivity of future searches.

DOI: 10.1103/1vds-2cgh

I. INTRODUCTION

Continuous gravitational waves (CWs) are long-lasting and almost monochromatic gravitational waves (yet to be detected) that can be emitted by different sources, such as asymmetric (around their rotation axis) rotating neutron stars [1]. Searches for CWs can have different targets, such as known pulsars or unknown neutron stars in our Galaxy (commonly called all-sky searches).

In order to discern whether a dataset contains an astrophysical signal or just noise, a detection statistic that is compared to a threshold is commonly computed. One of these detection statistics is the $\mathcal{F}$-statistic [2,3], which is obtained after analytical maximization (over the four amplitude parameters that describe a typical CW signal) of the log-likelihood ratio. This detection statistic has been used in many CW searches (see [4] for a recent review). Due to the prohibitive computational cost of some searches, the data can be divided in many shorter segments, and a semicoherent version of the $\mathcal{F}$-statistic might be used [5].

The typical CW signal model includes parameters that for some searches are unknown, such as the rotational frequency or the sky position. These unknown parameters have to be explicitly explored with a template bank or with a stochastic sampling algorithm. The parameter-space metric is a second-order approximation that aims to predict the relative loss of signal power (also called mismatch) incurred when these searched parameters are not equal to the true parameters of a putative astrophysical signal [6].

The full coherent parameter-space metric for the (multi-detector) $\mathcal{F}$-statistic was first derived in [6]. The different metrics derived there are subject to some idealizations, such as (i) the data is assumed to have no gaps, i.e., a duty cycle of 100%; (ii) the noise floor of each detector, quantified in terms of the amplitude spectral density (ASD), is assumed to be constant over time. Furthermore, the semicoherent metric (cf. [5,7,8]) for the $\mathcal{F}$-statistic has so far been derived under the assumption of (iii) equal signal power over segments. However, realistic datasets typically have an overall duty cycle less than 100% (usually around ∼70%), and varying duty cycles and noise floors over time, as shown in Fig. 1 for the O3 observing run [9,10] of the Advanced LIGO gravitational-wave detectors located in Hanford (H1) and Livingston (L1) [11].

In this paper, we attempt to study the behavior of the $\mathcal{F}$-statistic parameter-space metrics when these assumptions do not hold and derive generalized expressions and implementations that take these effects into account.

*Contact author: jb.covas@uib.es

Published by the American Physical Society under the terms of the Creative Commons Attribution 4.0 International license. Further distribution of this work must maintain attribution to the author(s) and the published article's title, journal citation, and DOI. Open access publication funded by the Max Planck Society.

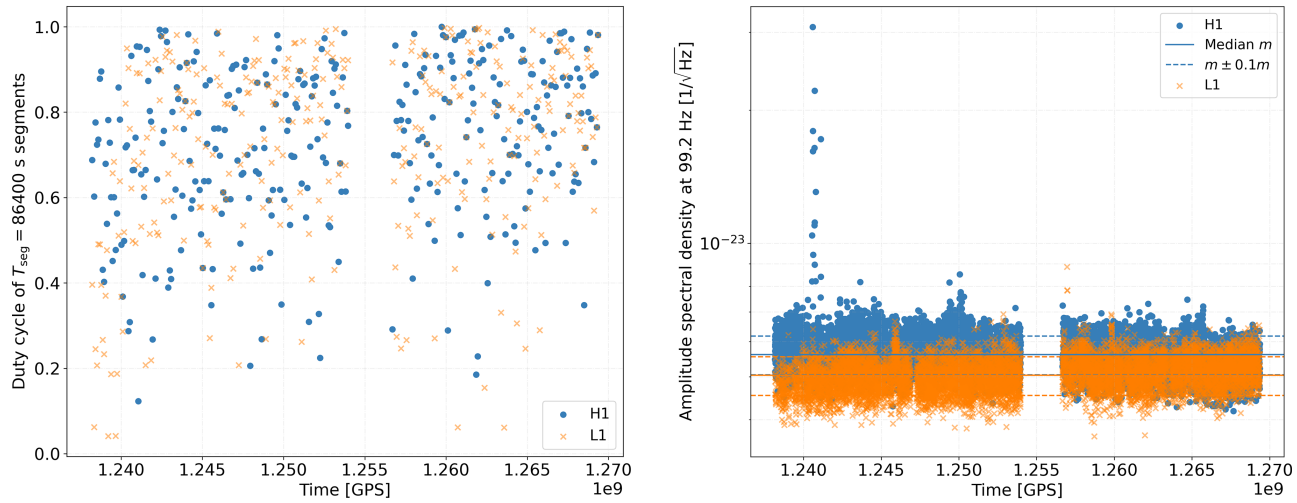

FIG. 1. The left plot shows the duty cycle of the O3 observing run for each segment of $T_{\mathrm{seg}} = 86\,400$ s as a function of the segment midtime for each detector. The right plot shows the amplitude spectral density (at 99.2 Hz) of the O3 observing run for each short Fourier transform (SFT) as a function of the SFT midtime, while the horizontal (dashed) lines show the median m ($m \pm 0.1$) for each detector. SFTs of 1800 s duration are used, which have been cleaned by a time-domain algorithm [12]. The different markers show the detectors H1 (blue circles) and L1 (orange crosses).

The parameter-space metric can be used to optimally construct a template grid [13,14], and since the sensitivity of some CW searches is bounded by a limited computational budget, placing templates in a more accurate way (due to more accurate mismatch predictions) is an important topic of research [15]. There are more reasons why obtaining more accurate parameter-space metrics is relevant for CW searches, such as (i) better analytical estimations of the uncertainty on the unknown parameters (see, for example, [16]) without having to carry out expensive Bayesian parameter estimation analyses; (ii) optimal setup algorithms (such as [15]) could indicate that discarding some fraction of the less sensitive data can be beneficial, and the resulting dataset would have a lower duty cycle, thus making the usage of more realistic metrics more relevant; (iii) use jump proposals (within Bayesian stochastic sampling algorithms such as [17]) based on the Fisher information matrix, which is proportional to the parameter-space metric; (iv) compare the resulting posteriors from a Bayesian stochastic sampling analysis with Fisher matrix predictions for validation tests.

The main results of this paper are (i) we derive an expression for the metric where data gaps and a varying noise floor are taken into account, and we implement this expression numerically; (ii) we present a new expression for a marginalized (over the unknown amplitude parameters) $\mathcal{F}$-statistic metric; (iii) we derive an expression for the semicoherent metric that properly takes into account the variability of the signal power across different segments by applying weights, and we derive the correct expression for detection statistics that are weighted, such as the one proposed in [18]. We test all of these new expressions and show that they are able to predict the mismatch more accurately than the previous expressions for realistic datasets.

This paper is organized in the following way: in Sec. II, we give an introduction to the $\mathcal{F}$-statistic and to parameter-space metrics; in Sec. III, we derive the expressions for the new generalized parameter-space metrics; in Sec. IV, we show the improved accuracy of the new metrics through diverse numerical tests; in Sec. V, we summarize the paper, present our conclusions, and advance some ideas for future research.

II. BACKGROUND

In this section, we introduce the basic framework and notation for the $\mathcal{F}$-statistic and its associated parameter-space metrics.

A. The $\mathcal{F}$-statistic

In order to detect CWs, we compare two main hypotheses about the data $x(t)$, where t is the time in the detector frame:

(i) noise hypothesis: the data only consist of Gaussian noise, $x(t) = n(t)$.
(ii) signal hypothesis: in addition to Gaussian noise, the data consist of a CW signal $s(t; \mathcal{A}_{\mathrm{s}}, \lambda_{\mathrm{s}})$ parametrized by four amplitude parameters $\mathcal{A}_{\mathrm{s}}$ and a number of phase-evolution parameters λ_{s}, i.e., $x(t) = n(t) + s(t; \mathcal{A}_{\mathrm{s}}, \lambda_{\mathrm{s}})$.

The CW signal can be expressed in terms of four basis functions h_μ in the form,

$$s(t; \mathcal{A}_{\mathrm{s}}, \lambda_{\mathrm{s}}) = \sum_{\mu=1}^{4} \mathcal{A}_{\mathrm{s}}^{\mu} h_\mu(\lambda_{\mathrm{s}}), \tag{1}$$

where $\mathcal{A}^\mu(h_0, \cos\iota, \psi, \phi_0)$ are the JKS amplitude parameters [2,19] depending on the overall signal amplitude h_0, polarization angles $\cos\iota$ and ψ, and the initial phase ϕ_0. The four basis functions h_μ are

$$h_1 = a(t)\cos\phi(t), \qquad h_2 = b(t)\cos\phi(t), \tag{2}$$

$$h_3 = a(t)\sin\phi(t), \qquad h_4 = b(t)\sin\phi(t), \tag{3}$$

where $a(t)$ and $b(t)$ are the antenna pattern functions (see [2,19]), and $\phi(t)$ is the phase of the signal in the detector frame, parametrized by the phase-evolution parameters λ such as the frequency f_0, spin-downs $f_1, f_2, \ldots$, the sky position, and (if applicable) binary orbital parameters.

The log-likelihood ratio between signal and noise hypotheses in this form is found to depend quadratically on the JKS amplitude parameters $\mathcal{A}^\mu$ of the template and can thus be analytically maximized (reducing the computational cost), which yields the well-known $\mathcal{F}$-statistic [2,3,20],

$$2\mathcal{F}(x;\lambda) = x_\mu \mathcal{M}^{\mu\nu} x_\nu, \tag{4}$$

with implicit summation over repeated $\mu, \nu = 1, \ldots, 4$. Here, we used the definitions,

$$x_\mu \equiv (x|h_\mu), \qquad \mathcal{M}_{\mu\nu} \equiv (h_\mu|h_\nu), \tag{5}$$

in terms of the multidetector scalar product [3,19], which for uncorrelated noise between detectors and a narrow band signal with flat noise floor in the signal band f can be written as

$$(x|y) \equiv 2\gamma\langle xy\rangle, \tag{6}$$

where we have defined the *data factor* γ as

$$\gamma \equiv \mathcal{S}^{-1} T_{\text{data}}, \tag{7}$$

with the total amount of data $T_{\text{data}} \equiv N_{\text{SFTs}} T_{\text{SFT}}$ in terms of the number N_{SFTs} and duration T_{SFT} of short Fourier transforms[1] (SFTs). The overall noise floor $\mathcal{S}$ at frequency f_0 is defined as

$$\mathcal{S}^{-1} \equiv \frac{1}{N_{\text{SFTs}}} \sum_{X\alpha} \mathcal{S}_{X\alpha}^{-1}, \tag{8}$$

in terms of the per-SFT power-spectral densities $\mathcal{S}_{X\alpha}$, where α is an index over SFTs of detector X. We define the time-averaging operation as

$$\langle xy\rangle \equiv \frac{1}{N_{\text{SFTs}}} \sum_{X\alpha}^{N_{\text{SFTs}}} \frac{w_{X\alpha}}{T_{\text{SFT}}} \int_{t_{X\alpha}-T_{\text{SFT}}/2}^{t_{X\alpha}+T_{\text{SFT}}/2} x_X(t) y_X(t) dt, \tag{9}$$

where the timestamps $t_{X\alpha}$ refer to the middle of an SFT. The per-SFT noise weights $w_{X\alpha}$ in this expression are defined as

$$w_{X\alpha} \equiv \frac{\mathcal{S}_{X\alpha}^{-1}}{\mathcal{S}^{-1}}, \tag{10}$$

with normalization,

$$\sum_{X\alpha} w_{X\alpha} = N_{\text{SFTs}}, \tag{11}$$

as can be seen from Eq. (8).

The $\mathcal{F}$-statistic follows a noncentral χ^2-distribution with an expectation value of

$$E[2\mathcal{F}(x;\lambda)] = 4 + \rho^2(\mathcal{A}_s, \lambda_s; \lambda), \tag{12}$$

with the noncentrality parameter defining the *signal power* $\rho^2(\mathcal{A}_s, \lambda_s; \lambda)$. In the perfect-match case, where the phase-evolution parameters of the template λ match those of the signal λ_s, the signal power can be expressed [22] as

$$\rho_0^2 \equiv \rho^2(\mathcal{A}_s, \lambda_s; \lambda_s) = (s|s) = h_0^2 \gamma g^2, \tag{13}$$

where we used the definition of the geometric response function g of [23], namely,

$$g^2(\hat{n}, \cos\iota, \psi) \equiv \alpha_1 A + \alpha_2 B + 2\alpha_3 C, \tag{14}$$

where $\hat{n}$ is the sky position, the amplitude angle factors $\alpha_k(\cos\iota, \psi)$ are defined as

$$\begin{aligned}
\alpha_1 &\equiv \frac{1}{4}(1+\cos^2\iota)^2\cos^2 2\psi + \cos^2\iota \sin^2 2\psi, \\
\alpha_2 &\equiv \frac{1}{4}(1+\cos^2\iota)^2\sin^2 2\psi + \cos^2\iota \cos^2 2\psi, \\
\alpha_3 &\equiv \frac{1}{4}(1-\cos^2\iota)^2 \sin 2\psi \cos 2\psi,
\end{aligned} \tag{15}$$

and $\gamma A \equiv \mathcal{M}_{11} = \mathcal{M}_{33}$, $\gamma B \equiv \mathcal{M}_{22} = \mathcal{M}_{44}$, and $\gamma C \equiv \mathcal{M}_{12} = \mathcal{M}_{34}$ are the (non-negligible) components of the (symmetric) antenna-pattern matrix $\mathcal{M}_{\mu\nu}$ defined in Eq. (5), with

$$A = \langle a^2\rangle, \qquad B = \langle b^2\rangle, \qquad C = \langle ab\rangle, \tag{16}$$

and the subdeterminant $D \equiv AB - C^2$.

Due to the high computational cost of wide-parameter-space CW searches, these typically use semicoherent methods, where the data will be divided into N_{seg} segments of duration T_{seg} each, and the four signal amplitude

[1]SFTs [21] are a typical format for the input data of CW searches. We assume stationary noise and constant antenna-pattern coefficients over the duration of each SFT.

parameters $\mathcal{A}^\mu$ are required to be constant only within each segment, resulting in the semicoherent $\hat{\mathcal{F}}$-statistic [5,24] as a sum of coherent $\mathcal{F}$-statistics over segments. This was generalized in [18] to the *weighted* semicoherent $\hat{\mathcal{F}}_{\mathrm{w}}$-statistic, defined as

$$2\hat{\mathcal{F}}_{\mathrm{w}}(x;\lambda) \equiv \sum_{\ell=1}^{N_{\mathrm{seg}}} w_\ell 2\mathcal{F}_\ell(x;\lambda), \tag{17}$$

where $\mathcal{F}_\ell$ is the coherent $\mathcal{F}$-statistic in segment ℓ and w_ℓ is the per-segment weight, with standard normalization (to have unit mean),

$$\sum_{\ell=1}^{N_{\mathrm{seg}}} w_\ell = N_{\mathrm{seg}}. \tag{18}$$

Dropping the per-segment weights recovers the classic semicoherent $\mathcal{F}$-statistic $2\hat{\mathcal{F}}(x;\lambda)$. As discussed in [18], a good choice of weights is empirically found as

$$w_\ell = k\gamma_\ell(A_\ell + B_\ell), \tag{19}$$

where the normalization k is fixed by Eq. (18). This (weighted) semicoherent $\mathcal{F}$-statistic follows a (*generalized*) noncentral χ^2-distribution with an expectation value of (assuming that all segments have 4 degrees of freedom)

$$\begin{aligned} E[2\hat{\mathcal{F}}_{\mathrm{w}}(x;\lambda)] &= \sum_{\ell=1}^{N_{\mathrm{seg}}} w_\ell(4+\rho_\ell^2) \\ &= 4N_{\mathrm{seg}} + \hat{\rho}_{\mathrm{w}}^2, \end{aligned} \tag{20}$$

where ρ_ℓ^2 is the signal power in segment ℓ, and we have defined the (weighted) semicoherent signal power $\hat{\rho}_{\mathrm{w}}^2$ as

$$\hat{\rho}_{\mathrm{w}}^2 \equiv \sum_{\ell=1}^{N_{\mathrm{seg}}} w_\ell \rho_\ell^2, \tag{21}$$

which reduces to the unweighted semicoherent signal power $\hat{\rho}^2$ when dropping the weights w_ℓ.

B. Parameter-space metrics

Due to the high computational cost of wide parameter-space CW searches, a grid of templates with finite spacing is used to cover the selected parameter-space region. For this reason, the values of the searched parameters will not be equal to the parameters of a possible astrophysical signal. The (coherent) mismatch μ describes the relative loss of signal power $\rho_0^2 \equiv \rho^2(\mathcal{A}_{\mathrm{s}}, \lambda_{\mathrm{s}}; \lambda_{\mathrm{s}})$ due to computing the coherent detection statistic at offset phase-evolution parameters $\lambda = \lambda_{\mathrm{s}} + \Delta\lambda$ with offset signal power $\rho_{\Delta\lambda}^2 \equiv \rho^2(\mathcal{A}_{\mathrm{s}}, \lambda_{\mathrm{s}}; \lambda)$, i.e.,

$$\mu \equiv 1 - \frac{\rho_{\Delta\lambda}^2}{\rho_0^2}, \tag{22}$$

which ranges from 0 (fully recovered signal power) to 1 (no recovered signal power).

The mismatch μ can be approximated by a Taylor expansion of the signal power around the signal parameters (where the mismatch attains a minimum of 0), keeping terms only up to second order [6],

$$m \equiv g_{ij}\Delta\lambda^i\Delta\lambda^j, \qquad \mu \approx m + \mathcal{O}(\Delta\lambda^3), \tag{23}$$

where g_{ij} is the parameter-space *metric* and i and j are indices over the phase-evolution parameters. The true mismatch μ of Eq. (22) is bound within [0, 1], while the metric-mismatch prediction m is quadratic in offsets $\Delta\lambda$ and can therefore be larger than one.

It has been shown that the metric mismatch m is typically a good approximation of the true mismatch μ of Eq. (22) up to mismatches of $\mu \lesssim 0.1$ [6,25], above which it starts to overestimate the true mismatch. The metric is useful to build template banks of given maximal mismatch and one can estimate the resulting number of templates $\mathcal{N}$ needed to cover a parameter-space region $\mathcal{R}$ by an expression of the form (neglecting boundary effects) [26],

$$\mathcal{N} \propto \int_{\mathcal{R}} \sqrt{\det(g_{ij})}\, d\lambda. \tag{24}$$

The most general form of the metric, as defined by Taylor-expanding Eq. (22), results in the $\mathcal{F}$-statistic metric $g_{ij}^{\mathcal{F}}(\cos\iota, \psi; \lambda)$, which depends on the subset $\{\cos\iota, \psi\}$ of the four signal amplitude parameters $\mathcal{A}_{\mathrm{s}}$. An explicit expression for this $\mathcal{F}$-statistic metric can be obtained [6] as

$$g_{ij}^{\mathcal{F}}(\cos\iota, \psi; \lambda) = \frac{\alpha_1 m_{1;ij} + \alpha_2 m_{2;ij} + 2\alpha_3 m_{3;ij}}{g^2}, \tag{25}$$

in terms of the amplitude angle functions $\alpha_i(\cos\iota, \psi)$ defined in Eq. (15), and the matrices,

$$\begin{aligned} m_{1;ij} &\equiv \langle a^2\partial_i\phi\partial_j\phi\rangle - \frac{A\langle ab\partial_i\phi\rangle\langle ab\partial_j\phi\rangle + B\langle a^2\partial_i\phi\rangle\langle a^2\partial_j\phi\rangle - 2C\langle a^2\partial_i\phi\rangle\langle ab\partial_j\phi\rangle}{D}, \\ m_{2;ij} &\equiv \langle b^2\partial_i\phi\partial_j\phi\rangle - \frac{A\langle b^2\partial_i\phi\rangle\langle b^2\partial_j\phi\rangle + B\langle ab\partial_i\phi\rangle\langle ab\partial_j\phi\rangle - 2C\langle ab\partial_i\phi\rangle\langle b^2\partial_j\phi\rangle}{D}, \\ m_{3;ij} &\equiv \langle ab\partial_i\phi\partial_j\phi\rangle - \frac{A\langle ab\partial_i\phi\rangle\langle b^2\partial_j\phi\rangle + B\langle ab\partial_i\phi\rangle\langle a^2\partial_j\phi\rangle - C[\langle b^2\partial_i\phi\rangle\langle a^2\partial_j\phi\rangle + \langle ab\partial_i\phi\rangle\langle ab\partial_j\phi\rangle]}{D}, \end{aligned} \tag{26}$$

where $\partial_i\phi \equiv \frac{\partial\phi}{\partial\lambda^i}$ are the partial phase derivatives for the phase-evolution parameters λ^i.

The signal amplitude parameters $\cos\iota$ and ψ are generally unknown; therefore, the practical usefulness of this metric is somewhat limited. One level of simplification consists in an amplitude-"average" form of the $\mathcal{F}$-statistic metric, $g^{\bar{\mathcal{F}}}_{ij}$, which was obtained [6] in the form,

$$g^{\bar{\mathcal{F}}}_{ij}(\lambda) = \frac{Bm_{1;ij} + Am_{2;ij} - 2Cm_{3;ij}}{2D}. \tag{27}$$

However, the most commonly-used approximation is the *phase metric* g^{ϕ}_{ij} (initially proposed in [27]), which is obtained by neglecting the signal amplitude modulation, resulting in the simpler expression,

$$g^{\phi}_{ij}(\lambda) = \langle \partial_i\phi\partial_j\phi\rangle - \langle\partial_i\phi\rangle\langle\partial_j\phi\rangle. \tag{28}$$

The semicoherent metric is typically obtained by averaging the coherent metrics over segments, namely,

$$\hat{g}_{ij} = \frac{1}{N_{\rm seg}}\sum_{\ell} g_{ij,\ell}, \tag{29}$$

which can be derived under the assumption of *constant per-segment signal power* (see, for example, [8] or [7]).

III. GENERALIZED PARAMETER-SPACE METRICS

In this section, we derive more general expressions for the various parameter-space metrics and discuss improvements in their implementation, in order to take into account data gaps and nonstationarities. This results in more accurate and robust parameter-space metrics, which will be tested numerically in Sec. IV.

A. Data gaps and varying noise floor

The metric expressions in Eqs. (25), (27), and (28) are typically computed numerically. However, current metric implementations in the $\mathcal{F}$-statistic context, including the main implementation in *UniversalDopplerMetric* of *lalsuite* [28], tend to implement the average Eq. (9) as a simple (unweighted) time average over the full observation span T of a segment, i.e., $\langle Q\rangle \approx 1/T\int_0^T Q(t)dt$, without taking into account data gaps or varying noise floors.[2] There is some support for differing noise-levels between detectors [see Eq. (59) in [6]], but this does not include noise-floor variations over time and is only implemented in the $\mathcal{F}$-statistic metrics $g^{\mathcal{F}}$ and $g^{\bar{\mathcal{F}}}$, not the phase metric g^{ϕ}.

[2]However, per-SFT summing and noise weighting for data gaps and nonconstant noise floor *has* been used previously for the cross-correlation statistic; see Sec. IV of [29].

In order to take into account data gaps and varying noise floors in the metric, we only need to use the full expression Eq. (9) for the weighted per-SFT average, which already incorporates these effects. We can see that SFTs with a higher noise floor $\mathcal{S}_{X\alpha}$ will contribute less to the metric integral. Therefore, adding noisier data (e.g., from a less sensitive previous observing run) will not improve the parameter-space resolution as much as the idealized metrics would predict [e.g., a linear scaling with the observation time for frequency resolution, for example, see Eq. (43) of [30]]. The effects of this more general implementation will be illustrated in Sec. IV.

B. New *marginalized* $\mathcal{F}$-statistic metric

As discussed in Sec. II B, the "average" $\mathcal{F}$-statistic metric $g^{\bar{\mathcal{F}}}$ in [6] is obtained as the midpoint between mismatch extrema of $g^{\mathcal{F}}$ over $\cos\iota, \psi$. A more natural approach consists of marginalizing the $\mathcal{F}$-statistic metric $g^{\mathcal{F}}(\cos\iota,\psi;\lambda)$ over the unknown amplitude parameters $\{\cos\iota,\psi\}$ using their physical ignorance priors $P(\cos\iota,\psi) = 1/\pi$, corresponding to isotropic axis orientation of the CW source (e.g., see [20]).

We define the *marginalized* $\mathcal{F}$-statistic metric $g^{\langle\mathcal{F}\rangle}$ as

$$\begin{aligned} g^{\langle\mathcal{F}\rangle}_{ij}(\lambda) &\equiv \langle g^{\mathcal{F}}_{ij}\rangle_{\cos\iota,\psi} \\ &= \frac{1}{\pi}\int_{-1}^{1} d\cos\iota \int_{-\pi/4}^{\pi/4} d\psi\, g^{\mathcal{F}}(\cos\iota,\psi;\lambda), \end{aligned} \tag{30}$$

which can be approximated (see Appendix B) as

$$g^{\langle\mathcal{F}\rangle}_{ij} \approx \frac{m_{1;ij} + m_{2;ij}}{A+B}. \tag{31}$$

This expression can be substantially more accurate than the "average" $\mathcal{F}$-statistic metric $g^{\bar{\mathcal{F}}}$, especially for short coherent segments, as shown in Sec. IV B, particularly Fig. 5.

The marginalized metric $g^{\langle\mathcal{F}\rangle}$ does not involve the inverse (sub)determinant D^{-1}, contrary to the "average" $g^{\bar{\mathcal{F}}}$ of Eq. (27), which can lead to numerical problems for short segments when $D \to 0$ (see [31]).

C. Generalized semicoherent metric

The usual expression Eq. (29) for the semicoherent metric, which was originally derived in [5] and is commonly found in the literature (e.g., see [7,8]), is derived under the assumption of constant signal power ρ^2_{ℓ} over all segments. However, this is not generally a good approximation due to varying (i) antenna-patterns A, B, C, (ii) data amounts $T_{\rm data}$, and (iii) noise-floors $\mathcal{S}$ over segments, as seen from Eq. (13) and Fig. 1.

A more accurate semicoherent metric can be derived by relaxing this assumption. The following derivation is written in terms of the general *weighted* semicoherent $\hat{\mathcal{F}}_{\rm w}$-statistic of Eq. (17), as the unweighted special case

can be recovered by simply dropping the per-segment weights w_ℓ.

Starting from the general mismatch definition given by Eq. (22), the semicoherent mismatch $\hat{\mu}_{\rm w}$ can be defined as[3]

$$\hat{\mu}_{\rm w} \equiv 1 - \frac{\hat{\rho}^2_{{\rm w}\Delta\lambda}}{\hat{\rho}^2_{\rm w0}}, \tag{32}$$

in terms of the offset and perfect-match semicoherent signal power of Eq. (21) using either offset $\rho^2_{\Delta\lambda;\ell}$ or perfect-match per-segment signal power $\rho^2_{0;\ell}$, respectively, and $\hat{\rho}^2_{\rm w0}$ is given in Appendix A. Using the per-segment mismatch μ_ℓ of Eq. (22), we can express the offset per-segment signal power as

$$\rho^2_{\Delta\lambda;\ell} = (1-\mu_\ell)\rho^2_{0;\ell}, \tag{33}$$

therefore,

$$\hat{\rho}^2_{{\rm w}\Delta\lambda} = \sum_\ell w_\ell \rho^2_{\Delta\lambda;\ell} = \hat{\rho}^2_{\rm w0} - \sum_\ell w_\ell \rho^2_{0;\ell}\mu_\ell, \tag{34}$$

and substituting into Eq. (32), we obtain

$$\hat{\mu}_{\rm w} = \frac{1}{N_{\rm seg}} \sum_{\ell=1}^{N_{\rm seg}} W_\ell \mu_\ell, \tag{35}$$

where we defined metric segment weights W_ℓ as

$$W_\ell \equiv \frac{N_{\rm seg} w_\ell \rho^2_{0;\ell}}{\hat{\rho}^2_{\rm w0}}, \tag{36}$$

with the usual weight normalization of $\sum_\ell W_\ell = N_{\rm seg}$. As mentioned before, the "classic" semicoherent metric expression given by Eq. (29) can be recovered under the assumption of constant (weighted) signal power over segments, i.e., $W_\ell = 1$.

Applying the metric expansion of Eq. (23) for the $\mathcal{F}$-statistic metric $g^{\mathcal{F}}_{ij,\ell}$, we find

$$\hat{\mu}_{\rm w} \approx \hat{g}^{\mathcal{F}}_{{\rm w};ij} \Delta\lambda^i \Delta\lambda^j + \mathcal{O}(\Delta\lambda^3), \quad \text{with} \tag{37}$$

$$\hat{g}^{\mathcal{F}}_{{\rm w};ij} \equiv \frac{1}{N_{\rm seg}} \sum_\ell W_\ell g^{\mathcal{F}}_{ij,\ell}. \tag{38}$$

As noted before in Sec. II B, however, this expression is not typically usable in practice, because both the metric weights W_ℓ and the $\mathcal{F}$-statistic metric $g^{\mathcal{F}}$ depend on the unknown signal amplitude parameters $\{\cos\iota, \psi\}$. The most natural approach again is to marginalize over them using physical priors, as discussed as in Sec. III B, and using the same marginalization approximation as before (see Appendix C for details), we obtain the general result,

$$\hat{g}_{{\rm w};ij}(\lambda) \approx \frac{1}{N_{\rm seg}} \sum_{\ell=1}^{N_{\rm seg}} \varpi_\ell g_{ij,\ell}(\lambda), \tag{39}$$

in terms of the marginalized *metric segment weights*,

$$\varpi_\ell \propto w_\ell \gamma_\ell (A_\ell + B_\ell), \tag{40}$$

with standard weight normalization $\sum_\ell \varpi_\ell = N_{\rm seg}$.

There are two important cases to distinguish, namely whether the underlying semicoherent statistic is weighted by w_ℓ or not (i.e., dropping w_ℓ in the above expressions). The explicit metric weights for two cases are, therefore,

$$\varpi_\ell = \begin{cases} k' w_\ell^2 & \text{for weighted } \hat{\mathcal{F}}_{\rm w}, \\ w_\ell & \text{for unweighted } \hat{\mathcal{F}}, \end{cases} \tag{41}$$

in terms of the segment weights w_ℓ given in Eq. (19).

For the unweighted $\hat{\mathcal{F}}$-statistic, the metric weights are therefore equal to the statistic weights w_ℓ derived in [18], while the metric weights for the weighted $\hat{\mathcal{F}}_{\rm w}$-statistic are proportional to the *squared* statistic weights.

A potential practical difficulty introduced by these metric weights is an additional sky-position dependency (via the antenna-pattern coefficients A, B), even if the per-segment metric itself was constant over the sky. This can complicate template-bank placement, but one would likely still reap benefits from using sky-marginalized weights instead, namely $\langle \varpi_\ell \rangle_{\rm sky} \propto \{\gamma_\ell^2, \gamma_\ell\}$ (for weighted and unweighted statistics, respectively), therefore still accounting for the variations in data-quality and quantity over segments illustrated in Fig. 1.

IV. NUMERICAL TESTS

In this section, we compare the accuracy of the (new) generalized parameter-space metrics derived in Sec. III to the (previous) idealized metrics, which ignore data gaps, nonconstant noise floors, and signal-power variability between segments. All calculations and simulations in this section use the C99 LALSuite library via the SWIGLAL Python interface [32].

A. Visual illustration

As a visual illustration of the improvements, Fig. 2 shows contour-levels of measured mismatch μ around an injected signal, overlaid with the metric ellipse for the (previous) idealized and the (new) generalized $\mathcal{F}$-statistic metric $g^{\mathcal{F}}$ of Eq. (25), computed for the exact injected signal parameters. The figure shows three examples, a fully coherent and two semicoherent short-segment $T_{\rm seg} = 0.1$ d statistics, using either unweighted or weighted $\mathcal{F}$-statistics.

[3]Note that *interpolating* semicoherent statistics require adjustments to the total mismatch, see [8,15], but those can be equally used with the expressions derived here.

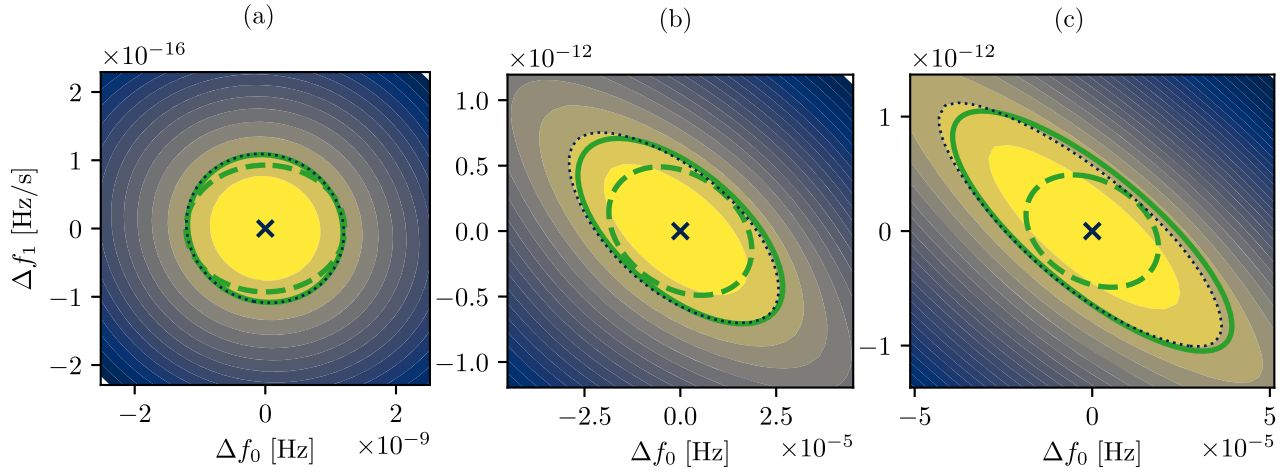

FIG. 2. Contour levels of *measured* mismatch μ (in steps of $\Delta\mu = 0.025$) in frequency f_0 and spin-down f_1 around an injected signal marked by "×" (with parameters $\cos\iota = 0.43$, $\psi = 0.01$ rad, $\alpha = 0.14$ rad, $\delta = -0.27$ rad, $f_0 = 100$ Hz, $f_1 = 6.4 \times 10^{-12}$ Hz/s at GPS time 1 218 673 431.5 s) in O2 + O3 data. Overlaid: (dotted dark blue) contour-line for measured-mismatch level $\mu = 0.05$ and the corresponding mismatch ellipses at $m = 0.05$ for the $\mathcal{F}$-statistic metric $g^{\mathcal{F}}$ using the previous idealized (dashed green) and the new generalized (solid green) metric, for (a) coherent $\mathcal{F}$-statistic, (b) semicoherent unweighted $\hat{\mathcal{F}}$-statistic, and (c) semicoherent weighted $\hat{\mathcal{F}}_{\mathrm{w}}$-statistic. Both semicoherent cases use short data segments of duration $T_{\mathrm{seg}} = 0.1$ d.

In all three cases, we observe improved agreement between the mismatch-ellipses of the new metrics with the corresponding measured-mismatch contour level.

B. Monte Carlo tests of metric-prediction error

In order to quantify the metric-prediction error, we compute the (symmetric) relative error ε between metric mismatch prediction m of Eq. (23) and the true mismatch μ of Eq. (22) (following [6,8,33]) as

$$\varepsilon \equiv 2\frac{\mu - m}{\mu + m} \in (-2, 2). \tag{42}$$

Note that the metric tends to increasingly overestimate the true mismatch μ at increasing mismatches $\mu \gtrsim 0.1$ (e.g., see [6,25]); therefore, these errors will typically have a bias towards negative values.

We compare the previous, idealized metric predictions to the new, generalized method of Sec. III C for the phase metric g^{ϕ}, the averaged $\mathcal{F}$-statistic metric $g^{\bar{\mathcal{F}}}$, and the full $\mathcal{F}$-statistic metric $g^{\mathcal{F}}$. Additionally, we show the prediction errors of the new marginalized $\mathcal{F}$-statistic metric $g^{\langle\mathcal{F}\rangle}$ that has no previous equivalent.

For these tests, we generate 100 simulated CW signals with random amplitude parameters drawn from their physical priors (see Sec. III B), isotropically distributed sky positions (using equatorial coordinates α and δ), frequency and spin-downs drawn uniformly from $f_0 \in [99.9, 100.1]$ Hz, $f_1 \in [-10^{-10}, 10^{-10}]$ Hz/s, $f_2 = [-10^{-17}, 10^{-17}]$ Hz/s^2, and binary parameters: projected semimajor axis $a_{\mathrm{p}} \in [10, 40]$ ls, period $P_{\mathrm{orb}} \in [15, 45]$ d, eccentricity $e \in [0, 0.1]$, and argument of periapsis $\omega \in [0, 2\pi)$. We fix the time of ascending node t_{asc} and the reference time for frequency and spin-downs to the midtime of the dataset.

For each signal, we generate 100 parameter-space offsets $\Delta\lambda$, drawn uniformly within the $\mathcal{F}$-statistic metric ellipsoid $g^{\mathcal{F}}_{ij}(\lambda_{\mathrm{s}})d\lambda^i d\lambda^j \leq 0.2$ (cf. Sec. IV C of [34]), computed at each signal location λ_{s} (resulting in a total of 10 000 offsets $\Delta\lambda$).

Given an offset, we can measure the mismatch $\mu(\Delta\lambda)$ of Eq. (22) between the statistic at the signal parameters λ_{s} and the offset point $\lambda_{\mathrm{s}} + \Delta\lambda$, and compare this to the metric prediction $m(\Delta\lambda) = g_{ij}(\lambda_{\mathrm{s}})\Delta\lambda^i\Delta\lambda^j$ via the relative error Eq. (42).

We consider five different search statistics, namely fully coherent $\mathcal{F}$, long-segment ($T_{\mathrm{seg}} = 10$ d) semicoherent and short-segment ($T_{\mathrm{seg}} = 0.1$ d) semicoherent, both for the unweighted $\hat{\mathcal{F}}$ and weighted $\hat{\mathcal{F}}_{\mathrm{w}}$ statistics. For each search statistic, we consider four different search targets:

(a) *directed isolated* with offsets in $\{f_0, f_1, f_2\}$,
(b) *directed binary* with offsets in $\{f_0, a_{\mathrm{p}}, P_{\mathrm{orb}}, t_{\mathrm{asc}}\}$,
(c) *all-sky isolated* with offsets in $\{f_0, f_1, \alpha, \delta\}$, and
(d) *all-sky binary* with offsets in $\{f_0, \alpha, \delta, a_{\mathrm{p}}, P_{\mathrm{orb}}, t_{\mathrm{asc}}\}$.

We use public data from the O2 and O3 observing runs [9,10,35] of the Advanced LIGO detectors to construct realistic datasets in terms of their distribution of SFT timestamps and noise ASD values. Each of the simulated CW signals is generated with duty cycles and ASD values corresponding to those O2/O3 datasets, but since we generate signals without noise (as required for metric tests), the fluctuating ASD values are used as *assumed* noise-floors when computing the $\mathcal{F}$-statistics [via Eq. (4)].

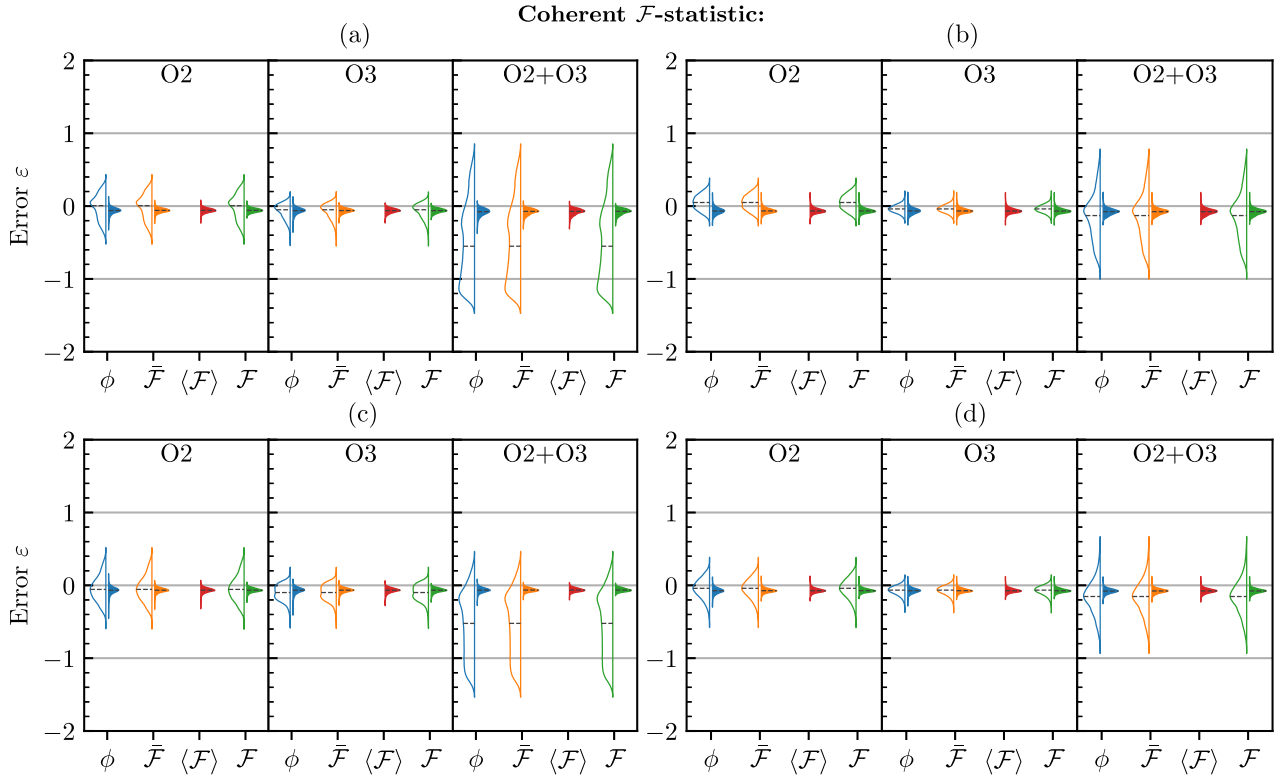

FIG. 3. Distributions of relative errors ε of Eq. (42) for metric mismatch predictions for different coherent $\mathcal{F}$-statistic searches: (a) directed isolated, (b) directed binary, (c) all-sky isolated, and (d) all-sky binary, using different datasets: O2, O3, or O2+O3-combined, and metrics: phase metric g^{ϕ}, averaged $\mathcal{F}$-statistic metric $g^{\bar{\mathcal{F}}}$, marginalized $\mathcal{F}$-statistic metric $g^{\langle\mathcal{F}\rangle}$, and the full $\mathcal{F}$-statistic metric $g^{\mathcal{F}}$. Each half-violin shows the error distribution over $\mathcal{O}(10^4)$ injections for one metric, where the left half (empty) uses the previous *idealized* metric while the right half (filled) uses the new *generalized* metric implementation discussed in Sec. III. The dashed vertical lines indicate the distribution median.

1. Coherent search

For the fully coherent $\mathcal{F}$-statistic search, the resulting distributions of the metric prediction error ε compared to the measured mismatch are shown in Fig. 3. We observe a general improvement of the metric prediction errors in the new generalized metric implementation compared to the previous idealized one, as the distribution mass is closer to zero (with a slight negative bias due to the known metric-mismatch overestimate mentioned earlier). Especially the big data gap between O2 and O3 causes large errors in the idealized metric computation for O2+O3, where this gap cannot be properly taken into account. We also note that all four different (generalized) metrics (i.e., g^{ϕ}, $g^{\bar{\mathcal{F}}}$, $g^{\langle\mathcal{F}\rangle}$, and $g^{\mathcal{F}}$) show very similar errors in all cases, which can be understood from the very long coherence time, where the $\mathcal{F}$-statistic metric is expected to converge to the phase-metric as previously discussed in [6,8].

2. Long-segment $T_{\mathrm{seg}} = 10$ d semicoherent search

For the long-segment $T_{\mathrm{seg}} = 10$ d semicoherent searches (unweighted and weighted) the metric-prediction error distributions are shown in Fig. 4. Similar to the coherent case, we see a general improvement of mismatch prediction accuracy by the new generalized metrics, which is most pronounced for the combined O2+O3 dataset due to the different noise levels in these two runs, which the idealized metric cannot take into account.

3. Short-segment $T_{\mathrm{seg}} = 0.1$ d semicoherent search

The error distributions for the short-segment $T_{\mathrm{seg}} = 0.1$ d semicoherent searches are presented in Fig. 5, which display a number of interesting features: (1) Much bigger differences between the different metric types, and especially a poor performance of the phase g^{ϕ} and averaged $g^{\bar{\mathcal{F}}}$ metrics, which is likely related to effects discussed previously in [6] (e.g., see Figs. 3 and 4). We also note that the $\mathcal{F}$-statistic itself is somewhat suboptimal for such short segments as first discussed in [31]. (2) A marked improvement from the averaged $g^{\bar{\mathcal{F}}}$ metric to the new marginalized $g^{\langle\mathcal{F}\rangle}$ metric derived in Sec. III B, which in all cases seems to perform virtually identically to the full $\mathcal{F}$-statistic metric $g^{\mathcal{F}}$. This is likely related to the degeneracy in gravitational-wave polarization information for short segments and the related problems discussed in [31], which marginalization

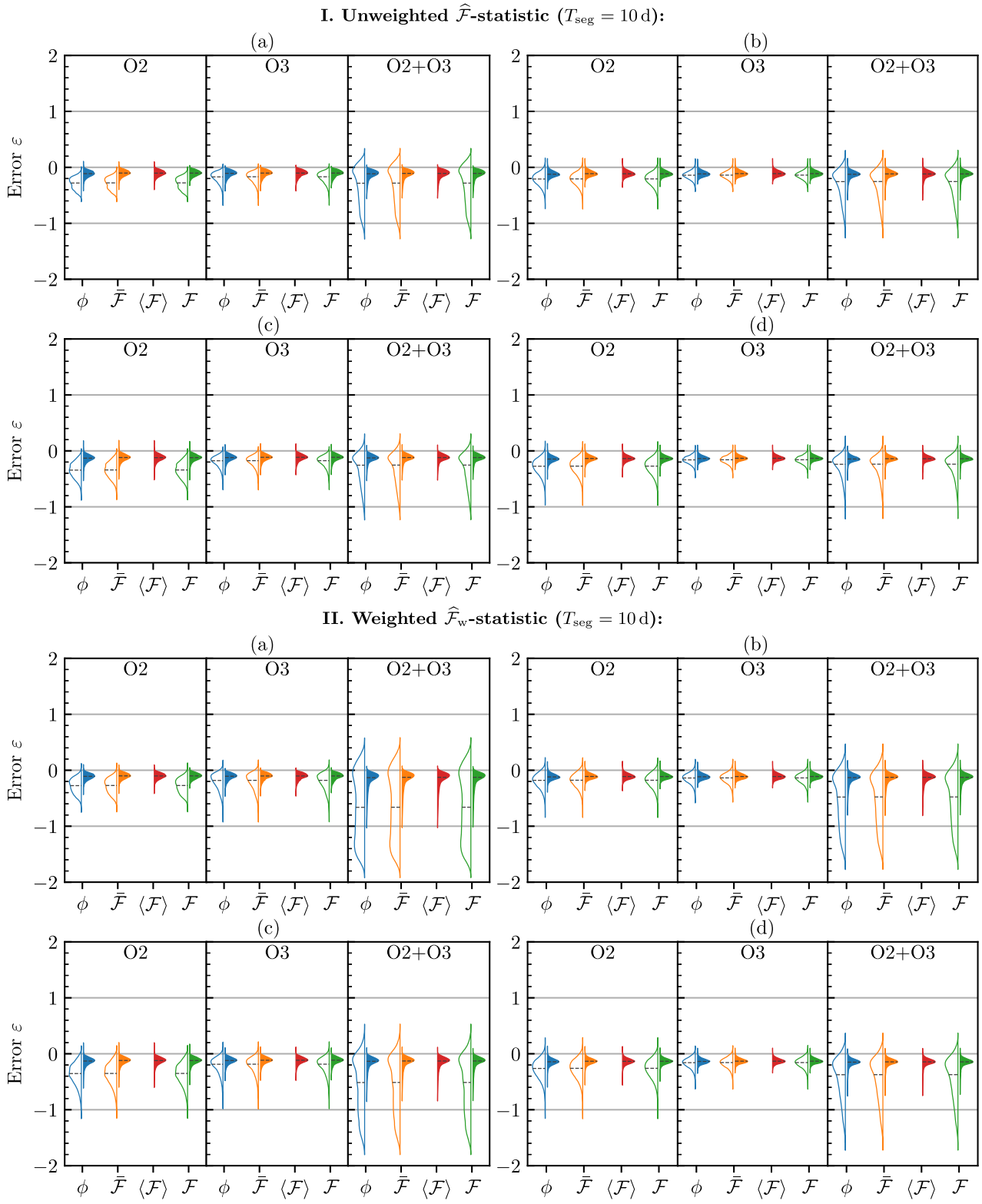

FIG. 4. Same as Fig. 3, for semicoherent searches with segments of duration $T_{\mathrm{seg}} = 10$ d. The top 2×2 block (I) is for the unweighted $\widehat{\mathcal{F}}$-statistic, with phase metric $\hat{g}^{\phi}$, averaged $\mathcal{F}$-statistic metric $\hat{g}^{\bar{\mathcal{F}}}$, marginalized $\mathcal{F}$-statistic metric $\hat{g}^{\langle\mathcal{F}\rangle}$, and the full $\mathcal{F}$-statistic metric $\hat{g}^{\mathcal{F}}$. The bottom 2×2 block (II) is for the weighted $\widehat{\mathcal{F}}_{\mathrm{w}}$-statistic, with phase metric $\hat{g}^{\phi}_{\mathrm{w}}$, averaged $\mathcal{F}$-statistic metric $\hat{g}^{\bar{\mathcal{F}}}_{\mathrm{w}}$, marginalized $\mathcal{F}$-statistic metric $\hat{g}^{\langle\mathcal{F}\rangle}_{\mathrm{w}}$, and the full $\mathcal{F}$-statistic metric $\hat{g}^{\mathcal{F}}_{\mathrm{w}}$. (a) directed isolated, (b) directed binary, (c) all-sky isolated, and (d) all-sky binary.

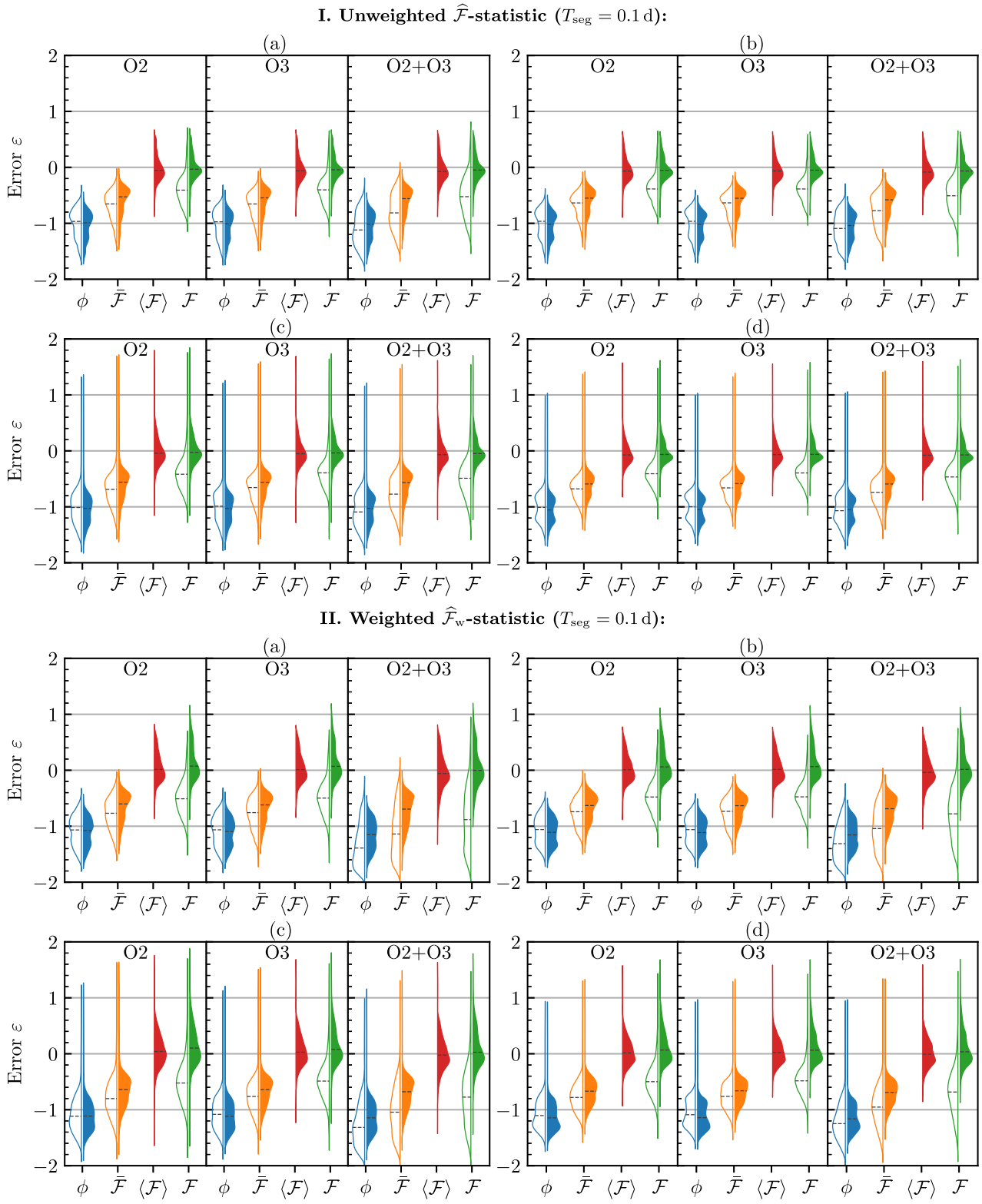

FIG. 5. Same as Fig. 3, for semicoherent searches with short segments of duration $T_{\rm seg} = 0.1$ d. The top 2×2 block (I) is for the unweighted $\widehat{\mathcal{F}}$-statistic, with phase metric $\hat{g}^{\phi}$, averaged $\mathcal{F}$-statistic metric $\hat{g}^{\bar{\mathcal{F}}}$, marginalized $\mathcal{F}$-statistic metric $\hat{g}^{\langle\mathcal{F}\rangle}$, and the full $\mathcal{F}$-statistic metric $\hat{g}^{\mathcal{F}}$. The bottom 2×2 block (II) is for the weighted $\widehat{\mathcal{F}}_{\rm w}$-statistic, with phase metric $\hat{g}^{\phi}_{\rm w}$, averaged $\mathcal{F}$-statistic metric $\hat{g}^{\bar{\mathcal{F}}}_{\rm w}$, marginalized $\mathcal{F}$-statistic metric $\hat{g}^{\langle\mathcal{F}\rangle}_{\rm w}$, and the full $\mathcal{F}$-statistic metric $\hat{g}^{\mathcal{F}}_{\rm w}$. (a) directed isolated, (b) directed binary, (c) all-sky isolated, and (d) all-sky binary.

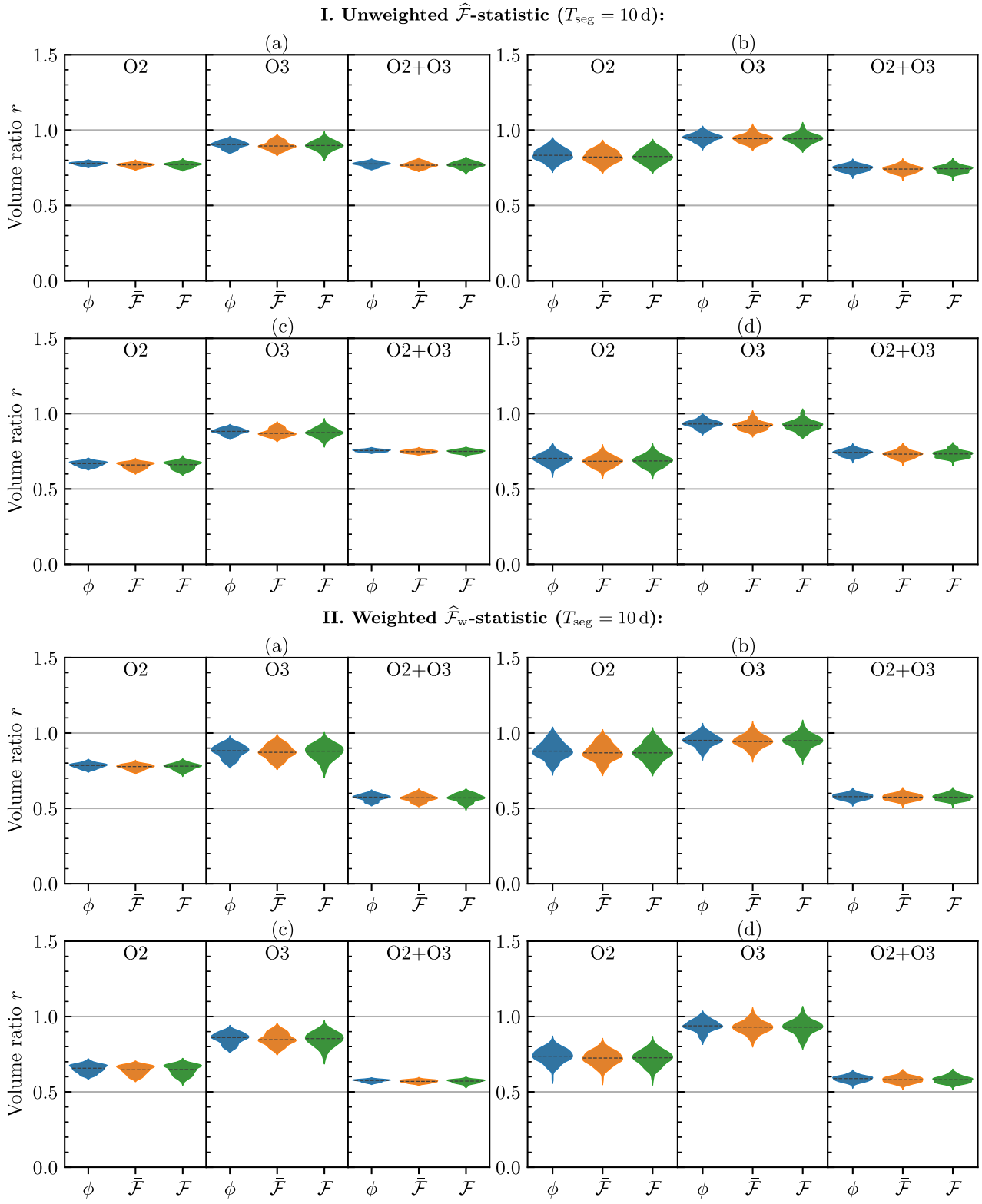

FIG. 6. Distributions of metric ellipse-volume ratio r of Eq. (43) for different semicoherent $\mathcal{F}$-statistic searches with segments of duration $T_{\mathrm{seg}} = 10$ d: (a) directed isolated, (b) directed binary, (c) all-sky isolated, and (d) all-sky binary, using different datasets: O2, O3, or O2 + O3-combined, and metrics: phase metric g^{ϕ}, averaged $\mathcal{F}$-statistic metric $g^{\bar{\mathcal{F}}}$, and the full $\mathcal{F}$-statistic metric $g^{\mathcal{F}}$.

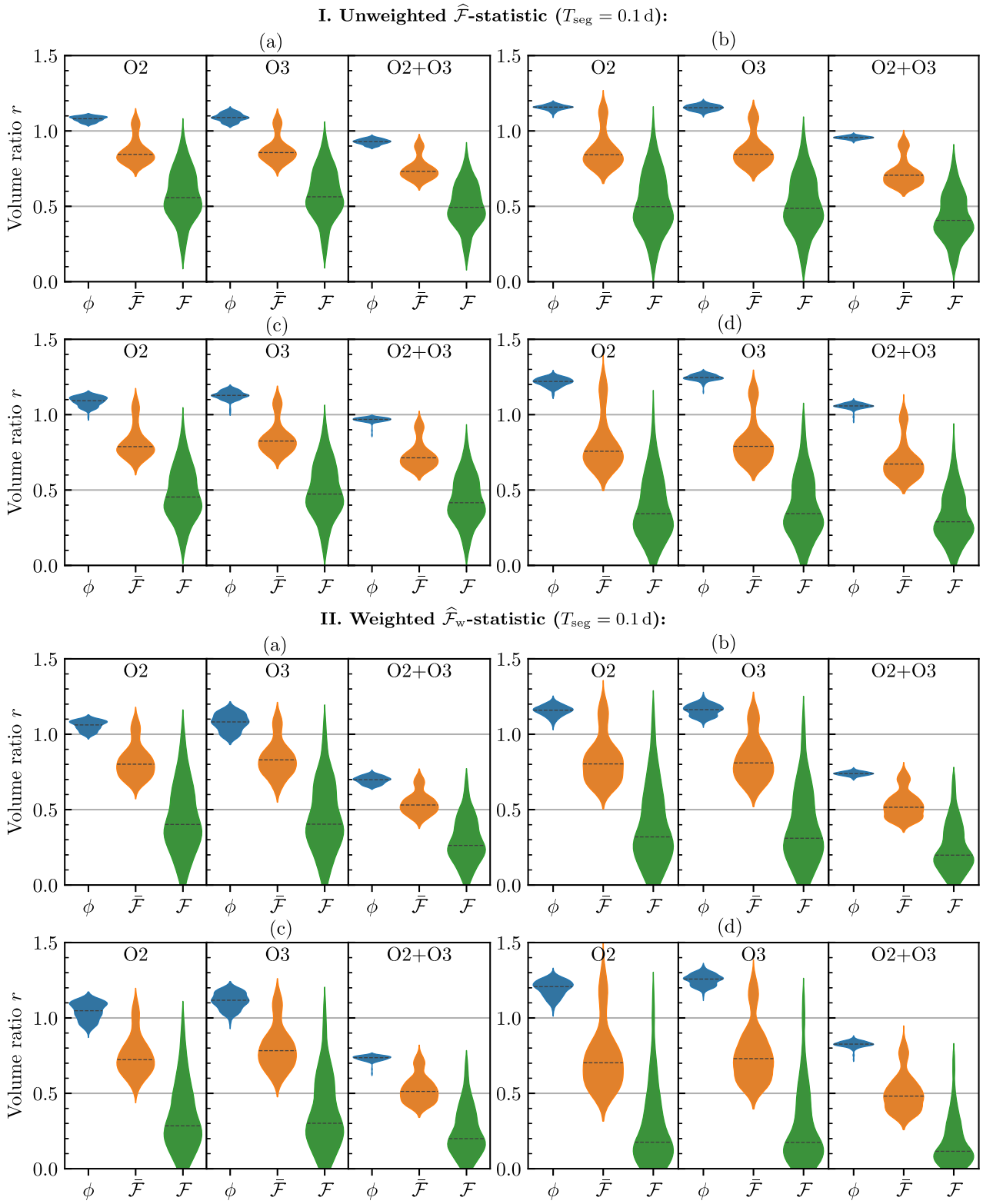

FIG. 7. Distributions of metric ellipse-volume ratio r of Eq. (43) for different semicoherent $\mathcal{F}$-statistic searches with short segments of duration $T_{\mathrm{seg}} = 0.1$ d: (a) directed isolated, (b) directed binary, (c) all-sky isolated, and (d) all-sky binary, using different datasets: O2, O3, or O2 + O3-combined, and metrics: phase metric g^{ϕ}, averaged $\mathcal{F}$-statistic metric $g^{\bar{\mathcal{F}}}$, and the full $\mathcal{F}$-statistic metric $g^{\mathcal{F}}$.

over physical priors seems to elegantly avoid; see also [23]. (3) A larger spread of relative errors (and tails) especially in the all-sky cases (c), (d), likely due to the metric not being constant even for small offsets $\Delta\lambda$, as shown, for example, in Fig. 14 of [6]. This can probably be avoided by choosing better sky coordinates, e.g., see [25], but is beyond the scope of this paper, and unrelated to the new metric approximation.

C. Effects on metric ellipse volumes

It is interesting to consider the effects of the generalized metric calculations of Sec. III on the metric-ellipse volume $V \propto 1/\sqrt{\det g}$, as this affects the total number of templates $\mathcal{N}$ required at a certain mismatch via Eq. (24). We therefore compute the metric ellipse-volume ratio r between the previous (idealized) g_{prev} and the new (generalized) g_{new} metrics as

$$r \equiv \frac{V_{\text{prev}}}{V_{\text{new}}} = \sqrt{\frac{\det g_{\text{new}}}{\det g_{\text{prev}}}}. \tag{43}$$

A larger metric-ellipse volume corresponds to a lower template density, and therefore to a smaller number of templates, as seen in Eq. (24); therefore, $r < 1$ corresponds to an expected reduction in number of templates with the new metric implementation, while $r > 1$ would indicate an expected increase.

We compute this ratio for the phase metric g^{ϕ}, the average $\mathcal{F}$-statistic metric $g^{\bar{\mathcal{F}}}$, and the $\mathcal{F}$-statistic metric $g^{\mathcal{F}}$, while the new marginalized metric $g^{\langle\mathcal{F}\rangle}$ has no previous implementation to compare to.

We only consider the semicoherent cases here, as full-dataset fully coherent searches are only computationally feasible when following up small numbers of interesting candidates in small parameter-space regions, where the question of the number of templates is irrelevant.

The results for the long-segment ($T_{\text{seg}} = 10$ d) semicoherent searches are shown in Fig. 6. We observe very similar results for the different metric types, namely an overall increase in metric ellipse volume (thereby reduction of expected number of templates) with the new generalized metrics.

The short-segment semicoherent searches are presented in Fig. 7. Here, we observe large differences between the three different metric types, but as we saw in the corresponding metric-prediction errors in Fig. 5, the phase-metric g^{ϕ} accuracy is quite poor for these short segments, and to some extent also the averaged $\mathcal{F}$-metric $g^{\bar{\mathcal{F}}}$. Therefore the result on the most accurate $\mathcal{F}$-statistic metric $g^{\mathcal{F}}$ is most significant here, which again shows a (substantial) reduction in expected number of templates from the generalized metric calculations compared to the previous idealized ones.

One can understand this general trend from the fact that taking into account of data-gaps and varying noise-floors amounts to a reduction in the effective coherence time, which would decrease the metric resolution compared to the idealized metrics that ignore these effects.

V. CONCLUSIONS

In this paper, we have generalized the expressions for the parameter-space metrics related to the $\mathcal{F}$-statistic. We have shown that for realistic datasets with data gaps and a varying noise floor the idealized expressions can fail to predict the shape and size of the $\mathcal{F}$-statistic mismatch correctly, and that the new generalized expressions are more accurate. We have presented a new metric approximation describing a polarization-marginalized $\mathcal{F}$-statistic metric $g^{\langle\mathcal{F}\rangle}$, which seems to improve accuracy and robustness compared to the averaged $\mathcal{F}$-statistic metric $g^{\bar{\mathcal{F}}}$. We have further derived a more accurate semicoherent metric that properly takes into account the variability of signal power across segments by using weights, and we have also extended the metric expression for weighted semicoherent statistics. We have shown that these new generalized metrics better predict the measured mismatches of the actual $\mathcal{F}$-statistic when used on realistic datasets including gaps and varying noise floors.

One downside of the new generalized metric expressions is a higher computational cost required to compute them, due to the need to integrate SFT by SFT, which might complicate their application in cases where many different metrics need to be computed, such as in an injection campaign with thousands of signals.

We have also found that the new metrics on realistic datasets (like the O2 and O3 observing runs) tend to reduce the expected number of required templates and thereby, the computing cost of searches using these metrics.

Here, we have only explored metrics for the classic $\mathcal{F}$-statistic, which was recently found to be quite suboptimal, especially for short segments [23,31]. It would therefore be very interesting to investigate what metric expressions one obtains for these new short-segment statistics, and how those would be related to the marginalized $\mathcal{F}$-statistic metric $g^{\langle\mathcal{F}\rangle}$. It might also be interesting to investigate the parameter-space metric of the detection statistic that includes a non-Gaussian line hypothesis such as [36].

ACKNOWLEDGMENTS

This project has received funding from the European Union's Horizon 2020 research and innovation programme under the Marie Sklodowska-Curie Grant Agreement No. 101029058. This work has utilized the ATLAS computing cluster at the MPI for Gravitational Physics Hannover. This research has made use of data or software obtained from the Gravitational Wave Open Science

Center [37], a service of the LIGO Scientific Collaboration, the Virgo Collaboration, and KAGRA [38,39].

DATA AVAILABILITY

The data that support the findings of this article are openly available [38,39].

APPENDIX A: WEIGHTED SEMICOHERENT SIGNAL POWER

Let us look in more detail at the (perfect-match) weighted semicoherent signal power $\hat{\rho}^2_{\mathrm{w}0}$ of Eq. (21), by inserting the per-segment matched signal power $\rho^2_{0;\ell}$ of Eq. (13), which leads to

$$\begin{aligned}\hat{\rho}^2_{\mathrm{w}0} &= \sum_\ell w_\ell \rho^2_{0;\ell} \\ &= h_0^2 \sum_\ell w_\ell \gamma_\ell (\alpha_1 A_\ell + \alpha_2 B_\ell + 2\alpha_3 C_\ell). \end{aligned} \tag{A1}$$

Using Eq. (7), we can see that semicoherent data factor $\hat{\gamma}$ is self-consistently defined as

$$\hat{\gamma} \equiv \mathcal{S}^{-1} T_{\mathrm{data}} = \sum_\ell \gamma_\ell, \tag{A2}$$

where $\mathcal{S}$, defined in Eq. (8), and T_{data} now refer to the full dataset over all segments. We can therefore write the weighted signal power Eq. (A1) in the form,

$$\hat{\rho}^2_{\mathrm{w}0} = h_0^2 \hat{\gamma} \hat{g}^2_{\mathrm{w}}, \tag{A3}$$

where we defined the (weighted) semicoherent geometric response function as

$$\hat{g}^2_{\mathrm{w}} \equiv \alpha_1 \hat{A}_{\mathrm{w}} + \alpha_2 \hat{B}_{\mathrm{w}} + 2\alpha_3 \hat{C}_{\mathrm{w}}, \tag{A4}$$

in terms of the (weighted) semicoherent antenna-pattern coefficients,

$$\begin{aligned}\hat{\gamma}\hat{A}_{\mathrm{w}} &\equiv \sum_\ell w_\ell \gamma_\ell A_\ell, \\ \hat{\gamma}\hat{B}_{\mathrm{w}} &\equiv \sum_\ell w_\ell \gamma_\ell B_\ell, \\ \hat{\gamma}\hat{C}_{\mathrm{w}} &\equiv \sum_\ell w_\ell \gamma_\ell C_\ell. \end{aligned} \tag{A5}$$

As expected, the above weighted expressions reduce to the standard semicoherent forms when dropping the weights w_ℓ.

APPENDIX B: AMPLITUDE-MARGINALIZING THE COHERENT $\mathcal{F}$-STATISTIC METRIC

In order to marginalize the $\mathcal{F}$-statistic metric $g^{\mathcal{F}}_{ij}$ of Eq. (25) over $\cos\iota, \psi$, we start by writing it more compactly as

$$g^{\mathcal{F}}_{ij}(\cos\iota, \psi; \lambda) = \sum_{k=1}^{3} m_{k;ij}(\lambda) \frac{\underline{\alpha}_k(\cos\iota, \psi)}{g^2(\cos\iota, \psi; \lambda)}, \tag{B1}$$

where for convenience of notation, we defined $\underline{\alpha}_1 \equiv \alpha_1$, $\underline{\alpha}_2 \equiv \alpha_2$ and $\underline{\alpha}_3 \equiv 2\alpha_3$. With the marginalization integrals over $\cos\iota, \psi$ of Eq. (30), we can write

$$g^{\langle\mathcal{F}\rangle}_{ij}(\lambda) \equiv \langle g^{\mathcal{F}}_{ij} \rangle_{\cos\iota,\psi} = \sum_{k=1}^{3} m_{k;ij}(\lambda) K_k(\lambda), \tag{B2}$$

in terms of the three marginalization integrals K_k, for which we propose the approximation,

$$K_k(\lambda) \equiv \left\langle \frac{\underline{\alpha}_k}{g^2} \right\rangle_{\cos\iota,\psi} \approx \frac{\langle \underline{\alpha}_k \rangle_{\cos\iota,\psi}}{\langle g^2 \rangle_{\cos\iota,\psi}}, \tag{B3}$$

replacing the average of the ratio by the ratio of averages. We will test the accuracy of this approximation numerically in Appendix D. We can use the known averages (e.g., [19]) of $\langle \alpha_1 \rangle_{\cos\iota,\psi} = \langle \alpha_2 \rangle_{\cos\iota,\psi} = 2/5$ and $\langle \alpha_3 \rangle_{\cos\iota,\psi} = 0$, to obtain $\langle g^2 \rangle_{\cos\iota,\psi} = \frac{2}{5}(A + B)$ from Eq. (14), and therefore,

$$K_1 \approx K_2 \approx \frac{1}{A + B}, \qquad K_3 \approx 0. \tag{B4}$$

Inserting this approximation into Eq. (B2), we now find

$$g^{\langle\mathcal{F}\rangle}_{ij} \approx \frac{m_{1;ij} + m_{2;ij}}{A + B}, \tag{B5}$$

as stated in Eq. (31).

APPENDIX C: AMPLITUDE MARGINALIZATION OF SEMICOHERENT METRICS

Here, we consider the amplitude-marginalization of the most general semicoherent metric $\hat{g}^{\mathcal{F}}_{\mathrm{w};ij}$ of Eq. (38) for (weighted) $\mathcal{F}$-statistics. We can write this amplitude-marginalized metric as

$$\begin{aligned}\hat{g}^{\langle\mathcal{F}\rangle}_{\mathrm{w};ij} &\equiv \langle \hat{g}^{\mathcal{F}}_{\mathrm{w};ij} \rangle_{\cos\iota,\psi} \\ &= \frac{1}{N_{\mathrm{seg}}} \sum_\ell \langle W_\ell g^{\mathcal{F}}_{ij,\ell} \rangle_{\cos\iota,\psi} \\ &= \sum_{k=1}^{3} \sum_{\ell=1}^{N_{\mathrm{seg}}} w_\ell m_{k;ij,\ell} \left\langle \frac{\rho^2_{0;\ell}}{\hat{\rho}^2_{\mathrm{w}0}} \frac{\underline{\alpha}_k}{g^2_\ell} \right\rangle_{\cos\iota,\psi}, \end{aligned} \tag{C1}$$

where in the last line, we substituted the metric weights W_ℓ of Eq. (36) and the per-segment $\mathcal{F}$-statistic metric $g^{\mathcal{F}}_{ij,\ell}$ of Eq. (B1). Using the explicit signal-power expression Eq. (13) with Eq. (A3) of Appendix A, this leads to

$$\hat{g}^{\langle\mathcal{F}\rangle}_{\mathrm{w};ij} = \sum_{k\ell} w_\ell m_{k;ij,\ell} \frac{\gamma_\ell}{\hat{\gamma}} K_{\mathrm{w};k}, \tag{C2}$$

where we defined [similar to the coherent case given by Eq. (B3)] the marginalization integrals $K_{\mathrm{w};k}$, for which we propose the approximation,

$$K_{\mathrm{w};k} \equiv \left\langle \frac{\alpha_k}{\hat{g}^2_{\mathrm{w}}} \right\rangle_{\cos\iota,\psi} \approx \frac{\langle \alpha_k \rangle_{\cos\iota,\psi}}{\langle \hat{g}^2_{\mathrm{w}} \rangle_{\cos\iota,\psi}}, \tag{C3}$$

with the result in the same form as in Appendix B,

$$K_{\mathrm{w};1} \approx K_{\mathrm{w};2} \approx \frac{1}{\hat{A}_{\mathrm{w}} + \hat{B}_{\mathrm{w}}}, \qquad K_{\mathrm{w};3} \approx 0. \tag{C4}$$

Putting this together with Eq. (C2), we obtain the approximation,

$$\begin{aligned} \hat{g}^{\langle\mathcal{F}\rangle}_{\mathrm{w};ij} &\approx \sum_\ell w_\ell \frac{\gamma_\ell}{\hat{\gamma}} \frac{m_{1;ij,\ell} + m_{2;ij,\ell}}{\hat{A}_{\mathrm{w}} + \hat{B}_{\mathrm{w}}} \\ &\approx \sum_\ell \left(w_\ell \frac{\gamma_\ell}{\hat{\gamma}} \frac{A_\ell + B_\ell}{\hat{A}_{\mathrm{w}} + \hat{B}_{\mathrm{w}}} \right) g^{\langle\mathcal{F}\rangle}_{ij,\ell}, \end{aligned} \tag{C5}$$

where in the last line, we used the coherent marginalized $\mathcal{F}$-statistic metric $g^{\langle\mathcal{F}\rangle}_{ij,\ell}$ of Eq. (31). We can see that the weight factor multiplying $g^{\langle\mathcal{F}\rangle}_{ij,\ell}$ corresponds to the (marginalized) metric segment weights ϖ_ℓ given in Eq. (40), namely,

$$\varpi_\ell \equiv k' w_\ell \gamma_\ell (A_\ell + B_\ell), \tag{C6}$$

with normalization,

$$k' = \frac{N_{\mathrm{seg}}}{\hat{\gamma}(\hat{A}_{\mathrm{w}} + \hat{B}_{\mathrm{w}})}, \tag{C7}$$

satisfying the normalization condition, $\sum_\ell \varpi_\ell = N_{\mathrm{seg}}$. Therefore, we can write

$$\hat{g}^{\langle\mathcal{F}\rangle}_{\mathrm{w};ij} \approx \frac{1}{N_{\mathrm{seg}}} \sum_\ell \varpi_\ell g^{\langle\mathcal{F}\rangle}_{ij,\ell}, \tag{C8}$$

as stated in Eq. (39).

In order to see that this form of the result also holds true for the phase metric, we first note that

$$\begin{aligned} \langle W_\ell \rangle_{\cos\iota,\psi} &= N_{\mathrm{seg}} w_\ell \left\langle \frac{\rho^2_{0,\ell}}{\hat{\rho}^2_{\mathrm{w}0}} \right\rangle_{\cos\iota,\psi} \\ &\approx N_{\mathrm{seg}} w_\ell \frac{\gamma_\ell}{\hat{\gamma}} \frac{\langle g^2_\ell \rangle}{\langle g^2_{\mathrm{w}} \rangle} \\ &= N_{\mathrm{seg}} \frac{w_\ell \gamma_\ell (A_\ell + B_\ell)}{\hat{\gamma}(\hat{A}_{\mathrm{w}} + \hat{B}_{\mathrm{w}})} \\ &= \varpi_\ell, \end{aligned} \tag{C9}$$

and therefore, the amplitude-marginalized weighted phase-metric is also approximated in the form,

$$\begin{aligned} \hat{g}^{\langle\phi\rangle}_{\mathrm{w};ij} &\equiv \langle g^\phi_{\mathrm{w};ij} \rangle_{\cos\iota,\psi} = \frac{1}{N_{\mathrm{seg}}} \sum_\ell \langle W_\ell \rangle g^\phi_{ij,\ell} \\ &\approx \frac{1}{N_{\mathrm{seg}}} \sum_\ell \varpi_\ell g^\phi_{ij,\ell}, \end{aligned} \tag{C10}$$

as stated in Eq. (39).

APPENDIX D: TESTING THE AMPLITUDE MARGINALIZATION APPROXIMATION

We perform numerical tests for the two cases of the coherent approximation given by Eq. (B4) of Appendix B as well as the semicoherent weighted case of Eq. (C4) of Appendix C. In these tests, we compare the true values, computed numerically, to the approximations.

Given K_3 is approximated as 0, we cannot compute a standard relative error; instead, we chose a common approximation "scale" of $K_0 \equiv 1/(A+B)$ to compute the relative importance of the absolute deviations in the sum in Eq. (B2), namely,

$$\varepsilon_1 \equiv \frac{K_1 - K_0}{K_0}, \qquad \varepsilon_2 \equiv \frac{K_2 - K_0}{K_0}, \qquad \varepsilon_3 \equiv \frac{K_3}{K_0}. \tag{D1}$$

We have made the same definitions for the semicoherent weighted case, substituting K_k and ε_k by $K_{\mathrm{w};k}$ and $\varepsilon_{\mathrm{w};k}$.

Figure 8 shows histograms of these relative deviations computed over randomly chosen sky-positions for different data spans. We see that this approximation tends to only introduce small errors on the order of a few percent for observation times of a day and longer. However, for shorter observations such as $T_{\mathrm{data}} = 1/4$ days, we see that this approximation is less precise, and a different approach might be needed, which is postponed to future work.

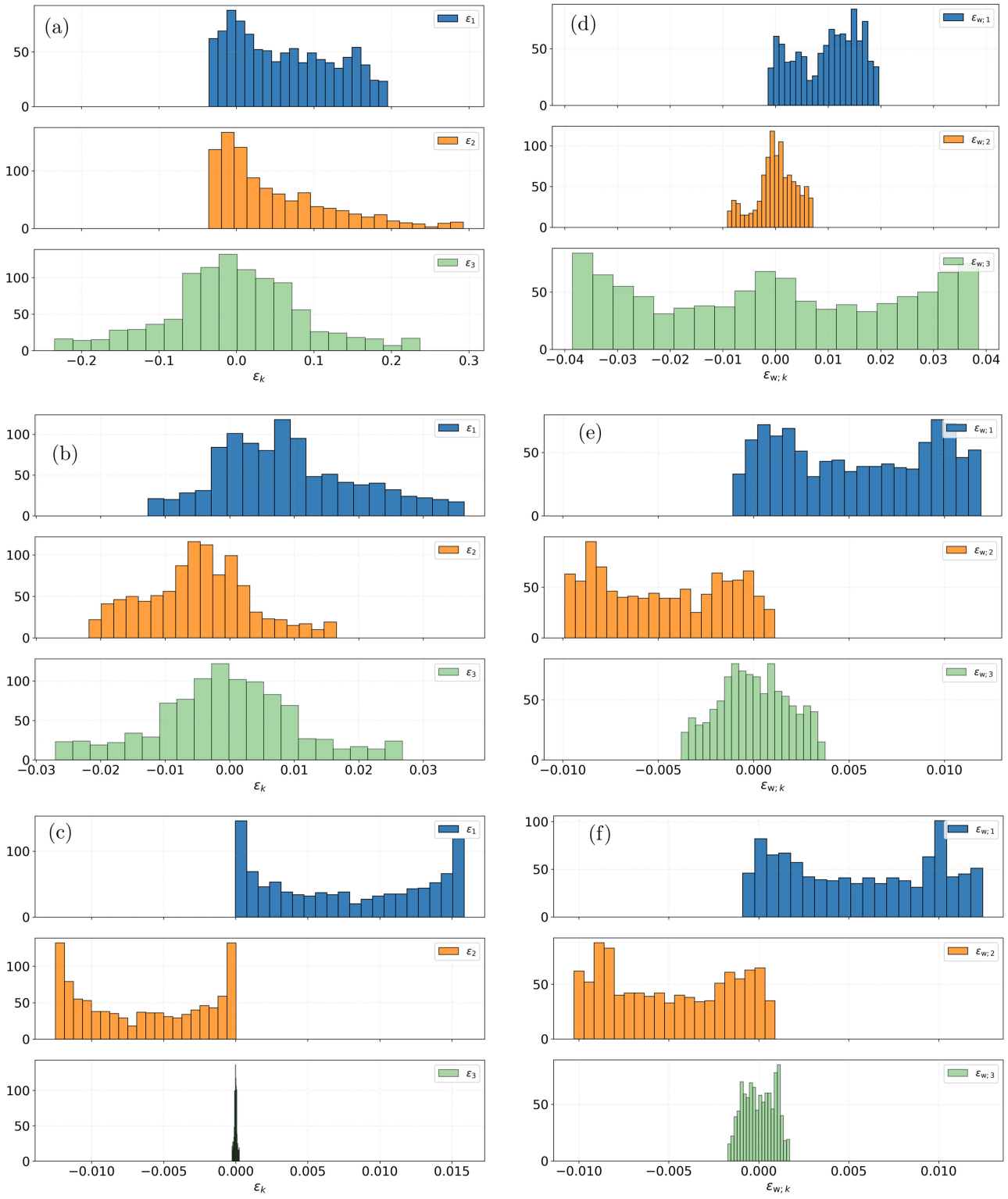

FIG. 8. Histogram showing ε_k, defined in Eq. (D1). The 1000 simulated signals of each histogram are isotropically distributed over the sky. For the left column, the antenna pattern matrix coefficients have been obtained with 1800 s SFTs without gaps from the H1 and L1 detectors with constant and equal noise floors covering (from top row to bottom) 0.25 days (a), 1.2 days (b), and 146 days (c). For the right column, the antenna pattern matrix coefficients have been obtained with 1800 s SFTs from the H1 and L1 detectors belonging to the O3 observing run that have been modified with a time-domain cleaning algorithm [12] with a segment time of (from top row to bottom) $T_{\mathrm{seg}} = 900$ s (d), $T_{\mathrm{seg}} = 1.2$ days (e), and $T_{\mathrm{seg}} = 12.1$ days (f).

[1] K. Riles, Living Rev. Relativity **26**, 3 (2023).
[2] P. Jaranowski, A. Królak, and B. F. Schutz, Phys. Rev. D **58**, 063001 (1998).
[3] C. Cutler and B. F. Schutz, Phys. Rev. D **72**, 063006 (2005).
[4] K. Wette, Astropart. Phys. **153**, 102880 (2023).
[5] P. R. Brady and T. Creighton, Phys. Rev. D **61**, 082001 (2000).
[6] R. Prix, Phys. Rev. D **75**, 023004 (2007).
[7] H. J. Pletsch, Phys. Rev. D **82**, 042002 (2010).
[8] K. Wette, Phys. Rev. D **92**, 082003 (2015).
[9] LIGO Scientific Collaboration, Virgo Collaboration, and KAGRA Collaboration, The O3a data release, 10.7935/nfnt-hm34(2021).
[10] LIGO Scientific Collaboration, Virgo Collaboration, and KAGRA Collaboration, The O3b data release, 10.7935/pr1e-j706 (2021).
[11] LIGO Scientific Collaboration, Classical Quantum Gravity **32**, 074001 (2015).
[12] B. Steltner, M. A. Papa, and H.-B. Eggenstein, Phys. Rev. D **105**, 022005 (2022).
[13] R. Prix, Classical Quantum Gravity **24**, S481 (2007).
[14] B. Allen, Phys. Rev. D **104**, 042005 (2021).
[15] R. Prix and M. Shaltev, Phys. Rev. D **85**, 084010 (2012).
[16] M. Sieniawska and D. I. Jones, Mon. Not. R. Astron. Soc. **509**, 5179 (2021).
[17] J. S. Speagle, Mon. Not. R. Astron. Soc. **493**, 3132 (2020).
[18] P. B. Covas and R. Prix, Phys. Rev. D **106**, 084035 (2022).
[19] R. Prix, LIGO DCC T0900149-v6, 2010.
[20] R. Prix and B. Krishnan, Classical Quantum Gravity **26**, 204013 (2009).
[21] B. Allen and G. Mendell, LIGO DCC T040164, 2004.
[22] C. Dreissigacker, R. Prix, and K. Wette, Phys. Rev. D **98**, 084058 (2018).
[23] R. Prix, Classical Quantum Gravity **42**, 065006 (2025).
[24] R. Prix, S. Giampanis, and C. Messenger, Phys. Rev. D **84**, 023007 (2011).
[25] K. Wette and R. Prix, Phys. Rev. D **88**, 123005 (2013).
[26] G. Ashton and R. Prix, Phys. Rev. D **97**, 103020 (2018).
[27] P. R. Brady, T. Creighton, C. Cutler, and B. F. Schutz, Phys. Rev. D **57**, 2101 (1998).
[28] LIGO Scientific Collaboration, Virgo Collaboration, and KAGRA Collaboration, LALSuite, 10.7935/GT1W-FZ16 (2018).
[29] J. T. Whelan, S. Sundaresan, Y. Zhang, and P. Peiris, Phys. Rev. D **91**, 102005 (2015).
[30] J. Ming, B. Krishnan, M. A. Papa, C. Aulbert, and H. Fehrmann, Phys. Rev. D **93**, 064011 (2016).
[31] P. B. Covas and R. Prix, Phys. Rev. D **105**, 124007 (2022).
[32] K. Wette, SoftwareX **12**, 100634 (2020).
[33] P. Leaci and R. Prix, Phys. Rev. D **91**, 102003 (2015).
[34] P. B. Covas, R. Prix, and J. Martins, Phys. Rev. D **110**, 024053 (2024).
[35] LIGO Scientific Collaboration, Virgo Collaboration, and KAGRA Collaboration, doi: 10.7935/CA75-FM95 (2019).
[36] D. Keitel, R. Prix, M. A. Papa, P. Leaci, and M. Siddiqi, Phys. Rev. D **89**, 064023 (2014).
[37] gwosc.org
[38] LIGO Scientific Collaboration and Virgo Collaboration, SoftwareX **13**, 100658 (2021).
[39] LIGO Scientific Collaboration, Virgo Collaboration, and KAGRA Collaboration, Astrophys. J. Suppl. Ser. **267**, 29 (2023).